Numerical Comparison of Two-Body Regularizations

Toshio Fukushima
National Astronomical Observatory, Ohsawa, Mitaka, Tokyo 181-8588, Japan
Toshio.Fukushima@nao.ac.jp

ABSTRACT

We numerically compare four schemes to regularize a three-dimensional two-body problem under perturbations; the Sperling-Bürdet (S-B), the Kustaanheimo-Stiefel (K-S), and the Bürdet-Ferrandiz (B-F) regularizations and a three-dimensional extension of the Levi-Civita (L-C) regularization we developed recently. As for the integration time of the equation of motion, the least is the unregularized treatment, then the K-S, the extended L-C, the B-F, and the S-B regularizations. However, these differences become significantly small when the time to evaluate perturbations becomes dominant. As for the integration error after one close encounter, the K-S and the extended L-C regularizations give the least in the tie, next comes the S-B, then the B-F, and the unregularized scheme for the unperturbed orbits with the eccentricity less than 2. This order is unchanged significantly by various kinds of perturbations. As for the integration error of elliptic orbits after multiple orbital periods, the situation remains the same except for the rank of the S-B scheme, which varies from the best to the second worst depending on the length of integration and/or on the nature of perturbations. Also we confirm that the Kepler energy scaling enhances the performance of the unregularized, the K-S, and the extended L-C schemes. As a result, the K-S and the extended L-C regularizations with the Kepler energy scaling provide the best cost performance in integrating almost all the perturbed two-body problems.

Subject headings: celestial mechanics—methods: numerical

1. Introduction

The two-body regularization is an efficient tool to integrate perturbed two-body problems numerically. This is true not only in astrodymanics (Bond & Allman 1996) but also in N-body simulations (Aarseth 2003). Originally it was developed to avoid the numerical difficulty in integrating nearly parabolic orbits like those of comets. However, its effectiveness was confirmed even for nearly circular orbits (Arakida & Fukushima 2000). This is due to its better numerical stability than the unregularized Keplerian motion (Stiefel & Scheifele 1971).

There are four schemes of three-dimensional two-body regularization. They are, in the chronological order of publication, (1) the Sperling-Bürdet (S-B) regularization (Sperling 1961; Bürdet 1967, 1968), which is also known as the Bürdet-Heggie regularization in the field of N-body simulation (Heggie 1973), (2) the Kustaanheimo-Stiefel (K-S) regularization (Kustaanheimo & Stiefel 1965), (3) the Bürdet-Ferrandiz (B-F) regularization (Bürdet 1969; Ferrrandiz 1988), and (4) an extension of Levi-Civita (L-C) regularization which we developed recently (Fukushima 2007). See Table 1 of Fukushima (2007) for their summary.

Recently a simple technique called the Kepler energy scaling (Fukushima 2003) has become to be known to enhance the performance of orbit integrations with the minimum increase of computational labor. So we consider the three modifications, too; (5) the unregularized treatment with the Kepler energy scaling (Fukushima 2003), (6) the K-S regularization with the Kepler energy scaling (Fukushima 2004), and (7) the extended L-C regularization with the Kepler energy scaling described in Appendix B4 of Fukushima (2007).

In this report, we present numerical comparisons of these schemes together with the unregularized formulation in the light of their computational cost and performance. All the numerical experiments given here are conducted at a PC with an Intel Pentium M chip of 1.3 GHz clock, the used programming language is the COMPAQ Fortran 6.6B compiler under the MS Windows XP Pro SP2, and the computing environment is double precision with the machine epsilon of $2^{-53} \approx 1.11 \times 10^{-16}$.

2. Comparison

2.1. Computational Time

First we compare the computational cost. As a typical example, we evaluate the computational time to integrate the equations of motion of two-body problems under N-body perturbations. To be more realistic, we simulate the orbit integration of Icarus in the heliocentric coordinate system where we count the perturbations due to major planets and a group of massive asteroids, the heliocentric orbits of which are approximated by given Keplerian orbits. Refer Table 1 for the initial Keplerian elements of Icarus and Jupiter, the largest perturber, in the heliocentric ecliptic coordinate system at the epoch J2000.0.

We compare the seven schemes described in §1 as well as the unregularized treatment, namely the direct integration in Cartesian coordinates. For each of these formulations, we conduct a test integration of Icarus covering about one million years and measure its execution time. We confirm that the measured computational times do not depend on the initial conditions of Icarus including the initial eccentricity. The reason we choose an elliptic orbit as a test case is to run a long time integration so that we can ignore the effect of the initial overhead such as the transformation to the regularized variables.

It is obvious that the unregularized treatment without the Kepler energy scaling runs fastest. Then we plot the ratios of the computational time of the schemes relative to that of the fastest treatment as a function of the number of perturbers. See Figure 1, where we omit the curves for those with the scaling since the additional computation time due to the scaling is too small to be seen. Among the regularized schemes, the fastest is the K-S, next comes closely the extended L-C, then the B-F, and the S-B scheme as the slowest. When compared with the unregularized treatment, the regularizations require 33, 35, 38, and 62 % more computation time in the order of the K-S, the extended L-C, the B-F, and the S-B schemes if no perturbations are considered. These numbers reduce to 21, 22, 26, and 39%, respectively in the case of comets/asteroids in the solar system when the perturbations due to eight classic planets are considered.

The excess in computation times directly reflects the extra computational labor to transform the physical time and the position, the velocity, and the acceleration vectors in Cartesian coordinates to/from each set of the regularized variables and their derivatives with their own time-like arguments, the procedures of which are summarized in Table 1 of Fukushima (2007). However, these additional computational times do not depend on the nature of perturbations. Therefore, its ratio relative to the whole integration time decreases significantly when the time to evaluate perturbations becomes dominant as clearly shown in Figure 1.

2.2. Treatment of Close Encounter

Next we compare how succesfully the close encounters are treated by the regularization schemes. To do this, we examine the integration errors caused by experiencing a single close encounter while fixing the number of function calls to evaluate the acceleration during the encounter. Since the degree of difficulty of close encounters mainly depends on the nominal eccentricity, we measure the errors while changing the initial eccentricity. Refer Table 2 for the eccentricities we must face in dealing with small solar system bodies.

In order to accommodate with closed elliptic orbits and open parabolic and hyperbolic orbits together, we fix the pericenter distance, q, and use a finite fraction of the orbits. More specifically speaking, we integrate the orbits in a finite range of time such that the radius vector, r, is less than or equal to eight times the pericenter distance, i.e. $r \leq 8q$. See Figure 2 for some orbit curves used for the measurement. In the figure, the attached numbers show the eccentricity, e. As a result, the tested arcs of orbit are classified into two categories; those with $e \leq 7/9 = 0.7777\cdots$ and those

with $e > 7/9$. The former arcs are closed while the latter ones are open. In the former case, we start test particles from the apocenter and measure the integration errors at the next apocenter passage. In the latter case, we start test particles from a point when $r = 8q$ and measure the integration errors at the point when $r = 8q$ once again.

Let us begin by unperturbed orbits. Figure 3 shows the manner of error growth during the integration for an unperturbed orbit with the eccentricity, $e = 0.99$. As a numerical integrator, we adopt the fourth order Runge-Kutta method. The errors are those in the physical position vector, $\mathbf{x}$, measured by comparing with the analytical solution, and divided by q. We fix the integration step length measured in the independent variable of each scheme throughout the integration. In other words, the integrated positions in orbits are evenly distributed in the mean anomaly for the unregularized case, in the true anomaly for the B-F regularization, and in the eccentric anomaly for the other schemes. Also we set the fixed step lengths such that the total number of integration steps is 64. This number is unchanged whether the regularization scheme or the initial eccentricity is altered. In the figure, 'NR' stands for 'No Regularization' and '+S' means that the Kepler energy scaling is applied. Also we omit the curves of the extended L-C regularization with or without the Kepler energy scaling since they are practically the same as those of the K-S regularization with or without the scaling, respectively. It is obvious that the errors of unreguralized treatment increase significantly according as the time whether the Kepler energy scaling is applied or not. On the other hand, the errors of all the regularized formulations are roughly flat with respect to the time.

In order to evaluate the eccentricity dependence of the integration errors suffered by experiencing a single close encounter, we prepare Figure 4 plotting the integration errors at the endpoints as functions of eccentricity. As the horizontal axis of the figure, we choose not e but Brunnow's parameter (Colwell 1993), $\lambda \equiv (1-e)/(1+e)$, to express all the possible values of eccentricity, $0 \leq e < +\infty$, in a compact manner, i.e. $-1 \leq \lambda \leq +1$. Thus the kinks in graphs when $\lambda = 0.125$ are due to the change in the type of tested arcs of orbits connected to the critical value $e = 7/9$. In the figure, we omit the curves of extended L-C regularization whether the Kepler energy scaling is applied or not since the differences from the corresponding curves of the K-S scheme are hardly visible.

2.3. Reason of Differences

Figure 4 illustrates large differences among the tested formulations. To understand the reason, we note the fact that most of the numerical integrators are designed to follow orbits the time variability of which is well approximated by low order polynomials. For example, the fourth order Runge-Kutta method exactly reproduces the orbits except for the round-off errors if the time dependence of orbits is described as a fourth or lower order polynomial of the adopted time-like argument. Therefore, the differences in the integration errors are presumed to be caused by the differences in functional forms of main variables with respect to the time-like argument used by each formulation. For this purpose, we prepare Appendix describing the solution expressions of unperturbed Keplerian orbits in the regularized and unregularized formulations.

Let us examine the solution curves in detail. As for the unregularized treatment, its main variables exhibit nonuniform behaviours with respect to the physical time, t, especially when the orbit is nearly parabolic, namely when $\lambda \sim 0$. See Figures 5 and 6 illustrating the time dependence of the pericenter component, x, for various eccentricities. Cusped features of the curves near the pericenter passage, when $t = 0$, are eminent in the nearly parabolic cases. This is the main reason why the integration errors of the unregularized treatment are so large in Figure 4. On the other hand, when the orbit is almost rectilinear such as in the case $\lambda \sim -1$, the integration errors of the unregularized treatment reduce so drastically that the unregularized treatment provides the best performance. While, the main variables of the B-F regularizations, n_x and n_y, are sinusoidal curves with respect to its time-like argument, the true anomaly, f, whichever value the eccentricity takes as described in Appendix. This is the reason why the integration errors of the B-F regularization are almost independent on the eccentricity.

Next, let us focus our attention on the fact that the errors of the S-B, the K-S, and the extended L-C regularizations become drastically small in the

nearly parabolic region, $\lambda \sim 0$. In the parabolic limit where $\lambda = 0$, this is well understood since the regularized solutions in these schemes are expressed by at-most cubic polynomials with respect to their time-like argument, s. Refer Appendix A.2. Thus the fourth order Runge-Kutta method perfectly reproduces the orbit.

Then, how are the features in the non-parabolic case explained? In the elliptic case, the solutions of the main variables of all the above regularizations are of the form of harmonic oscillation. We recall a fact that the global truncation error of a sinusoidal motion with the angular frequency, ν, by a numerical integrator using a fixed step size, h, is in proportion to $(h\nu)^p$ where p is the order of the integrator. Appendix A.1 tells that the normalized angular frequency of the harmonic oscillation in the extended L-C and the S-B regularizations for elliptic orbits is $(\sqrt{1-e})/2$ and $\sqrt{1-e}$, respectively. While, the normalized angular frequency becomes unity in the B-F regularization. Then the ratio among the magnitude of integration errors of the B-F, the S-B, and the extended L-C regularizations as well as that of the K-S regularization becomes $1 : (1-e)^{p/2} : [(1-e)/4]^{p/2}$.

First, this ratio explains well the fact that, in Figure 4, the integration errors of the S-B and the B-F regularizations become the same in the limit of circular orbit, $e = 0$. Next, if we substitute $p = 4$ for the RK4 integrator, this ratio mostly explains the differences of these regularizations. See Figure 7 illustrating the curves of the S-B and the K-S regularizations with and without the Kepler energy scaling replotted in a log-log scale. The feature of their eccentricity dependence is well explained by a model curve based on the above explanation. Also a constant difference in logarithm between the S-B and the K-S regularizations precisely coincide with the prediceted value, $\log_{10} 4^2 \approx 1.2$.

On the other hand, the reason why the Kepler energy scaling improves the orbit integration was already reported in Fukushima (2003). In short, it is due to an on-the-fly correction of the integrated variables to satisfy a consistency condition among them. This mechanism works so efficiently that, in the case of nearly circular orbits, say when $\lambda > 2/3$, or $e < 0.2$, the unregularized treatment with the Kepler energy scaling becomes superior to the B-F and the S-B regularizations so as to be comparable with the K-S regularization. See Figure 4 again.

The above line of logic is almost applicable to the hyperbolic case if we interpret the sine and cosine functions with the arguments including s with the corresponding hyperbolic functions and take care that $e > 1$ in this case. Then the above ratio becomes $1 : (e-1)^{p/2} : [(e-1)/4]^{p/2}$. See Figure 7 again.

A decrease of integration errors is also achieved by reducing the step size, which results the increase in computational time. Therefore, we can rephrase the above statement as follows; in order to achieve the same integration precision at endpoints, the extended L-C and the K-S regularizations run twice faster than the S-B regularization. Also the S-B scheme requires $\sqrt{|1-e|}$ times fewer number of integration steps than the B-F one except for some highly hyperbolic cases seen in Figure 4.

2.4. Effect of Perturbations

Let us examine the effect of perturbations on the results obtained for unperturbed orbits in the previous subsection. We consider five kinds of perturbations; (1) the third body perturbation, (2) the general relativistic perturbation, (3) the air drag perturbation, (4) the radiation pressure perturbation, and (5) the nonspherical gravitational field perturbation. As for the third body perturbation, we choose a coordinate system the origin of which is the primary body, which we roughly call the heliocentric coordinate system by imagining cometary orbits in the solar system. Also we ignore the mass of the secondary body in the case of third body perturbation. Namely we deal with an elliptic restricted three-body problem in three-dimension.

The detailed explanation of the perturbation models are found in Appendix C of Fukushima (2005) except the case (4), where we assume that the acceleration due to the radiation pressure is given as

$$\mathbf{a}_{\mathrm{RP}} = c_{\mathrm{RP}}\mathbf{n}. \tag{1}$$

Here $\mathbf{n}$ is a unit vector in the direction from a radiation emitter, such as the Sun in the case of an artificial satellite orbitting around the Earth, and c_{RP} is a coefficient determined by the following three factors; (1) the distance from the emitter,

(2) the mass of the secondary body, (3) the cross section of the secondary body toward the direction of $\mathbf{n}$. For simplicity, we fix the direction vector as $\mathbf{n} = \mathbf{e}_y$, i.e. in the y-axis of the inertial coordinate system. Also we set $c_{\rm RP}$ a numerical constant on the order of 10^{-8} in the unit system, $\mu = q = 1$.

In all the tested cases, we set the initial Keplerian elements of the secondary body relative to the primary one the same as those of Icarus listed in Table 1 except the eccentricity, e. In order to make the maximum strength of perturbations roughly the same, we fix not a but q when e is altered. As for the third body perturbation, we choose the mass of the perturber as 10^{-3} in the unit system $\mu = 1$ and all the Keplerian elements of the third body with respect to the primary one the same as those of Jupiter as shown in Table 1. This is to resemble the orbit of a near-Earth object perturbed by Jupiter.

As for the general relativistic perturbation, we consider the post-Newtonian term only and set its nominal magnitude as 10^{-8} in order to resemble the Sun's general relativistic effect acting on Icarus. As for the air drag perturbation, we adopt a model with a constant drag coefficient for simplicity and set its nominal magnitude as 10^{-8}, which roughly represents the maximum drag of an artificial Earth satellite in low altitudes. As for the nonspherical gravitational field, we assume that it consists of only the spheroidal term with the coefficient $J_2 = 0.001$ in order to mimic the main perturbation effect on a low-altitude Earth orbiter. In this case we presume that the primary body rotates around its figure axis being set the same as the z-axis of the coordinate system.

In general, an exact solution is not available in the perturbed case. Then we measure the integration errors by comparing with a reference solution which we obtain separately in the same scheme by using the same integrator but adopting a halved step size. In the case of the fourth order Runge-Kutta method, the main error term is known to be in proportion to h^4 where h is the step size adopted. Then we obtain an accurate estimate of the integration error by the following formula;

$$\Delta\mathbf{x} \approx \left(\frac{16}{15}\right)\delta\mathbf{x}, \quad \delta\mathbf{x} \equiv \mathbf{x}_h - \mathbf{x}_{h/2}, \qquad (2)$$

where $\mathbf{x}_h$ and $\mathbf{x}_{h/2}$ are the position vector solutions obtained by setting the step size as h and $h/2$, respectively. For the regularized schemes using the time-like arguments other than t, we need another device to synchronize the errors;

$$\delta\mathbf{x} \approx \left(\mathbf{x}_h - \mathbf{x}_{h/2}\right) - \mathbf{v}_{h/2}\left(t_h - t_{h/2}\right), \qquad (3)$$

where t_h and $t_{h/2}$ are the physical time solutions obtained by setting the step size of the time-like argument as h and $h/2$, respectively. See §3 of Fukushima (2004).

Let us describe the differences we observe between the perturbed and unperturbed cases. First, we confirm that most of the features observed in Figures 4 and 7 are unchanged except for the following two cases; the third body perturnation and the J_2 perturbation for the nearly parabolic region, $\lambda \approx 0$. See Figure 8 for the closeup of the same curves as in Figure 4 but under the third body perturbation. In the parabolic limit, where $\lambda = 0$, the S-B regularization gives the least error. Also the K-S regularization give somewhat better results than the extended L-C one. This situation is unchanged by applying the Kepler energy scaling. However, the differences among the best five schemes shown in Figure 8 are small, say at most a factor 4. On the other hand, Figure 9 illustrates the same closeup for the J_2 perturbation. In this case, the superiority of the K-S and the extended L-C regularizations to the S-B ones is unchanged. In conclusion, the features we observe in the close encounter experiment of perturbed orbits are almost the same as that of unperturbed case.

2.5. Long-Term Error Growth

In N-body simulations, a bottle neck in the computation is to follow precisely the orbit evolution of a compact binary subsystem with a large eccentricity but the orbit of which is still elliptic. In astrodynamics, it is rare but nonzero to deal with highly eccentric orbits for a long time span. Then we examine how the integration errors of such an elliptic orbit grow with respect to time.

For this purpose, we select an unperturbed elliptic orbit with $e = 0.5$ and integrate it for about one thousand orbital periods. In order to accelerate the execution of experiments we replace the fourth order Runge-Kutta method by the tenth order imiplicit Adams method in the PECE (Predict, Evaluate, Correct, Evaluate) mode and fix the stepsize as 1/64 of the initial orbital period.

The starting tables for the Adams method are prepared by Gragg's extrapolation method with a tiny error tolerance. As an illustration, we plot the integration errors of all the tested schemes in Figure 10 as functions of the physical time, t. Again we omit the results for the extended L-C regularization whether the Kepler energy scaling is applied or not since their differences from the corresponding curves of the K-S regularizations are hardly seen.

The magnitude of errors are different scheme by scheme from the beginning. During the first several orbital periods, the highest precision is achieved by the K-S regularization. It is noteworthy that, at this stage, the Kepler energy scaling does not improve the precision of the K-S regularization significantly. Then comes the S-B, the B-F, the unregularized scheme with the Kepler energy scaling, and the worst is the unregularized treatment. These differences are mainly caused by the same reasons we find in the close encounter experiment; namely the difference in the functional forms of the main variables with respect to the adopted time-like argument and the difference in magnitude of the frequency of associated harmonic oscillation. Then how do these features change according with time?

Except the unregularized treatment which immediately reaches a plateau of errors of the order of unity, the curves obtained are categorized into two groups; those with a quadratically growing component and those with a linearly growing component. The former consists of the B-F regularization and the K-S and the extended L-C regularizations without the Kepler energy scaling. The latter contains the S-B regularization and the K-S and the extended L-C regularizations with the Kepler energy scaling. It is quite interesting that the S-B regularization exhibits a linear growth rate as the schemes with the Kepler energy scaling although its mechanism is unclear to the author. This difference in growth rate brings a large difference in the long run. See Figure 11 for the eccentricity dependence of the integration errors after 1024 orbital periods. At this timing, the S-B regularization provides better results than the K-S regularization for all the eccentricities.

Figures 10 and 11 may give an impression that the S-B regularization becomes superior to the K-S and the extended L-C regularizations in the long run, say after 1024 orbital periods. However, this is not always true. Figure 12 shows the perturbation type dependence of the integration errors of the S-B regularization for about one million orbital periods. As seen there, the performance of the S-B regularization is significantly degraded when the perturbations depend on the velocity such as the cases of the air drag perturbation and the general relativistic perturbation.

On the other hand, we confirm that the features of the other schemes observed in Figures 10 and 11 are mostly unchanged when the type of perturbations is altered. This means that the performance rank of the S-B regularization depends on both the time of comparison and the type of perturbation. For example, if we compare the short time performance, say the errors after a few hundreds orbital periods, the K-S regularization *without* the Kepler energy scaling is superior to the S-B regularization as seen in Figures 4. Under the perturbations independent on the velocity, this order is reversed in the long run say after some thousands revolutions. In this sense, we should say that the S-B regularization is fragile.

In any event, the superiority of the K-S and the extended L-C regularizations *with* the Kepler energy scaling is unchanged thanks to the fact that they share the properties that the initial errors are small and the errors grow almost linearly with respect to time.

2.6. Cost Performance Diagram

In order to examine the numerical stability and the total cost performance of the tested schemes for long orbit integrations, we integrate the same test orbit in the previous subsection while changing the step size in a wide range; from a few steps per period to some thousands steps per period. Figure 13 illustrates the errors after 1024 orbital periods as functions of the step size in a log-log scale. Once again we omit the results of the extended L-C regularization with and without the Kepler energy scaling since they are practically the same as the corresponding K-S regularization respectively. The horizontal axis of the figure shows the number of steps per orbital period. Since the computational time per each single step does not change significantly scheme by scheme as we learn from Figure 1, this number is almost in proportion to the computational time. On the other

hand, the vertical axis indicates the integration precision. Although these are the results for unperturbed orbits, we confirm that they remain the same under various kinds of perturbations for the indicated timing of comparison, i.e. after 1024 orbital revolutions. Then this diagram shows the cost performace of tested schemes in the sense that a scheme is of a high cost performance if its curve locates in the left lower place and vice versa.

Obviously the K-S regularization with the Kepler energy scaling as well as the extended L-C one with the same scaling is of the highest cost performance. Next comes the S-B regularization and the K-S regularization without the Kepler energy scaling in the tie. However, this is correct for the chosen timing, after 1024 orbital periods. If it is earlier, then the K-S regularization without the Kepler energy scaling ranks the second best and the S-B one does the third. If it is later, then the S-B regularization becomes the second best. In any term, the B-F regulzarization becomes the fourth, the unregularized formulation with the Kepler energy scaling ranks the fifth, and the unregularized treatment is the worst.

Besides the cost performance, the figure reveals two other aspects; the stability limit and the achievable precision. For each curve in the diagram, there is a certain lower limit of the number of steps per orbital period which assures a reliable integration. The smaller the number is, the more stable the scheme becomes. The figure shows that the number is 22 for the extended L-C and K-S regularizations with and without the Kepler energy scaling, 44 for the S-B and the B-F regularizations and the unregularized treatment with the Kepler energy scaling, and 48 for the unregularized treatment. Note that these numbers depend on the adopted numerical integrator.

Of course, this is the result obtained for the tested eccentricity, $e = 0.5$. Additional experiments indicate that the numerical values for the extended L-C, the K-S, the S-B, and the B-F regularizations are in proportional to $\sqrt{1-e}$. Thus the difference in the stability region is a direct result of the difference in the frequency of harmonic oscillation associated with the regularization; $(\sqrt{1-e})/2$ for the extended L-C and the K-S regularizations and $\sqrt{1-e}$ for the S-B and the B-F regularizations and the unregularized treatment.

On the other hand, the achievable precision of integration is indicated by the minimum of the integration error with respect to the step size. It is clear that the schemes with the Kepler energy scaling are of a higher achievable precision than those without it. This is mainly due to the facts (1) that the initial errors of the methods with the Kepler energy scaling can be reduced to the level of machine epsilon if an appropriate step size is chosen and (2) that the growth rate of their errors are small.

3. Conclusion

We compare various aspects of four existing schemes to regularize a three-dimensional two-body problem under perturbations; the Sperling-Bürdet (S-B) regularization also known as the Bürdet-Heggie regularization, the Kustaanheimo-Stiefel (K-S) regularization, the Bürdet-Ferrandiz (B-F) regularization, and a three-dimensional extension of the Levi-Civita (L-C) regularization we developed recently. Also we test the unregularized treatment, and the enhanced versions of the unregularized treatment, and the K-S and the extended L-C regularizations with the Kepler energy scaling.

First, the comparison of computational time indicates that a regularization requires 30-60 % extra time at most. However, this additional cost reduces to a negligible portion when the time to evaluate perturbations becomes large. Second, we compare the capability of close encounter. The highest performance is achieved by the K-S and the extendeded L-C regularizations with the Kepler energy scaling. The difference between them is negligiblly small. Next rank the K-S and the extendeded L-C regularizations without the scaling, then the S-B regularization, the B-F regularization, the unregularized treatment with the scaling, and the unregularized treatment without the scaling. This order is unchanged with respect to the nominal eccentricity except when the orbit is almost hyperbolically rectilinear. Third, we compare the long-term performance in elliptic orbits. The comparison in the initial errors, namely the errors after one orbital period, does reflect the result we obtained in the close encounter experiment. On the other hand, there is a significant difference in the maqnner of error growth. The

S-B regularizations and the schemes with the Kepler energy scaling grow linearly with respect to time while the other schemes grow faster, namely quadratically. This tendency is almost independent on the nature of perturbations for the first thousand orbital periods. However, the S-B regularization gives very poor result in the long run when the perturbations depend on the velocity. As a result, we conclude that the highest cost performance is realized by the K-S and the extended L-C regularizations with the Kepler energy scaling.

APPENDIX

A. Regularized and Unregularized Solutions of Keplerian Motion

In the below, we summarize the two-dimensional solutions of unperturbed two-body problems in the orbital plane expressed in the extended L-C, the S-B, and the B-F regularizations as well as the unregularized formulation. In this case, the solutions in terms of the extended L-C and the K-S regularizations reduces to that of the original L-C one by assigning zero values for the two components of the orbital angular momentum vector as $L_I = L_J = 0$ in the former and the third and the fourth components of the fictitious position and velocity vectors, $u_3 = u_4 = w_3 = w_4 = 0$, in the latter. Also, by taking the orbital plane as the x-y plane, we can nullify the z-components of the S-B variables as $z = P_z = 0$. Next, we make $P_y = 0$ by assuming that the positive x-axis in the physical space is in the direction of the pericenter. Further, we count from a pericenter passage all the time-like arguments; namely the physical time, t, for the unregularized treatment, the fictitious time, s, for the extended L-C, the K-S, and the S-B regularizations, and the true longitude, θ, for the B-F regularization. As a result, the time-like argument of the B-F regularization reduces to the true anomaly, f. In order to simplify the following expressions, we adopt a unit system such that $\mu = q = 1$. Some regularized variables remain constants in the unperturbed orbits as

$$K = \frac{e-1}{2}, \quad L = \sqrt{1+e}, \quad P_x = e, \tag{A1}$$

where K is the Kepler energy, L is the total orbital angular momentum, and P_x is the x-component of the Laplace vector. To recover the dimensioned expressions, we note that the dimensions of non-zero variables, which will appear in the below, are as follows; (1) u_1 and u_2 are of the dimension $\sqrt{q}$, (2) w_1 and w_2 are of the dimension $\sqrt{\mu}$, (3) x, y, and r are of q, (4) v_x and v_y are of $\sqrt{\mu/q}$, (5) ρ and σ are of $1/q$, (6) K is of μ/q, (7) L is of $\sqrt{\mu q}$, (8) P_x is of μ, (9) t is of $\sqrt{q^3/\mu}$, (10) s is of $\sqrt{q/\mu}$, and (11) e, f, n_x, n_y, m_x, and m_y are of no dimension.

A.1. Elliptic Orbit

First, we assume that the eccentricity, e, satisfies the condition, $0 \le e < 1$. Then, the nonconstant variables of the L-C regularized solution are the two-dimensional fictitious position vector, (u_1, u_2), the two-dimensional fictitious velocity vector, (w_1, w_2), and the physical time, t, as functions of the fictitious time, s, as

$$u_1(e,s) = \cos\left\{\frac{\left(\sqrt{1-e}\right)s}{2}\right\}, \quad u_2(e,s) = \sqrt{\frac{1+e}{1-e}}\sin\left\{\frac{\left(\sqrt{1-e}\right)s}{2}\right\},$$

$$w_1(e,s) \equiv \frac{du_1(e,s)}{ds} = \frac{-\sqrt{1-e}}{2}\sin\left\{\frac{\left(\sqrt{1-e}\right)s}{2}\right\},$$

$$w_2(e,s) \equiv \frac{du_2(e,s)}{ds} = \frac{\sqrt{1+e}}{2}\cos\left\{\frac{\left(\sqrt{1-e}\right)s}{2}\right\},$$

$$t(e,s) \equiv \int_0^s \left[u_1^2(e,s') + u_2^2(e,s')\right] ds' = \frac{\left(\sqrt{1-e}\right)s - e\sin\left\{\left(\sqrt{1-e}\right)s\right\}}{\left(\sqrt{1-e}\right)^3}. \tag{A2}$$

Although the above expressions of $u_2(e,s)$ and $t(e,s)$ seem to be singular due to a divisor, $\sqrt{1-e}$, they remain well-defined in the limit $e \to 1$.

Next, the nonconstat variables of the S-B regularized solution are the two-dimensional physical position vector, (x, y), the radius vector, r, the two-dimensional physical velocity vector, (v_x, v_y), and t as functions

of s. The solution expressions of x, y, and r are derived from those of u_1 and u_2 as

$$x(e,s) \equiv u_1^2(e,s) - u_2^2(e,s) = \frac{\cos\left\{\left(\sqrt{1-e}\right)s\right\} - e}{1-e},$$

$$y(e,s) \equiv 2u_1(e,s)u_2(e,s) = \sqrt{\frac{1+e}{1-e}}\sin\left\{\left(\sqrt{1-e}\right)s\right\},$$

$$r(e,s) \equiv u_1^2(e,s) + u_2^2(e,s) = \frac{1 - e\cos\left\{\left(\sqrt{1-e}\right)s\right\}}{1-e},$$

$$v_x(e,s) \equiv \frac{2\left[u_1(e,s)w_1(e,s) - u_2(e,s)w_2(e,s)\right]}{r(e,s)} = \frac{-\sqrt{1-e}\sin\left\{\left(\sqrt{1-e}\right)s\right\}}{1 - e\cos\left\{\left(\sqrt{1-e}\right)s\right\}},$$

$$v_y(e,s) \equiv \frac{2\left[u_1(e,s)w_2(e,s) + u_2(e,s)w_1(e,s)\right]}{r(e,s)} = \frac{(1-e)\sqrt{1+e}\cos\left\{\left(\sqrt{1-e}\right)s\right\}}{1 - e\cos\left\{\left(\sqrt{1-e}\right)s\right\}}, \tag{A3}$$

and that of $t(e,s)$ is the same as in the above. Again, all these expressions remain well-defined in the limit $e \to 1$.

As a by-product, the unregularized solution is given in parametric representations of x, y, v_x, v_y, and t by means of s as

$$x(e,t) \equiv x(s(e,t)), \quad y(e,t) \equiv y(s(e,t)), \quad v_x(e,t) \equiv v_x(s(e,t)), \quad v_y(e,t) \equiv v_y(s(e,t)), \tag{A4}$$

where the inverse function, $s(e,t)$, is not analytically expressed in terms of elementary functions but obtained by solving the universal Kepler's equation, $t(e,s) = t$, with respect to s. The detailed procedure to solve the equation for arbitrary value of e is described in Fukushima (1999), where the notations used, G and L, are to be translated as $(\sqrt{1+e})s$ and $(\sqrt{1+e})t$ in terms of the convention used in this Appendix, respectively.

Finally, the nonconstant variables of the B-F regularized solution are the two-dimensional unit position vector in the orbital plane, (n_x, n_y), the two-dimensional unit vector perpendicular to the former, (m_x, m_y), the inverse radius, ρ, its derivative with respect to f, σ, and t in terms of not s but the true anomaly, f, as

$$n_x(f) \equiv \frac{x}{r} = \cos f, \quad n_y(f) \equiv \frac{y}{r} = \sin f,$$

$$m_x(f) \equiv \frac{dn_x(f)}{df} = -\sin f, \quad m_y(f) \equiv \frac{dn_y(f)}{df} = \cos f,$$

$$\rho(e,f) \equiv \frac{1}{r} = \frac{1 + e\cos f}{1+e}, \quad \sigma(e,f) \equiv \frac{d\rho(f)}{df} = \frac{-e\sin f}{1+e},$$

$$t(e,f) \equiv \int_0^f \frac{df'}{L\rho^2(e,f')} = \frac{1}{\left(\sqrt{1-e}\right)^3}\left[f - 2\tan^{-1}\left(\frac{e\sin f}{1+\sqrt{1-e^2}+e\cos f}\right) - \frac{e\sqrt{1-e^2}\sin f}{1+e\cos f}\right]. \tag{A5}$$

This expression of $t(f)$ is effective for all the possible values of f in the range $-\infty < f < +\infty$ and remains well-defined in the limit $e \to 1$. Note that the solution expressions of n_x, n_y, m_x, and m_y are independent on e.

A.2. Parabolic Orbit

The solution expressions of the parabolic orbit are directly derived from those of the elliptic orbit by taking the limit $e \to 1$. In fact, the L-C regularized solutions become

$$u_1(1,s) = 1, \quad u_2(1,s) = \frac{s}{\sqrt{2}}, \quad w_1(1,s) = 0, \quad w_2(1,s) = \frac{1}{\sqrt{2}}, \quad t(1,s) = s + \frac{s^3}{6}, \tag{A6}$$

and the S-B regularized solutions become

$$x(1,s) = 1 - \frac{s^2}{2}, \quad y(1,s) = \sqrt{2}s, \quad r(1,s) = 1 + \frac{s^2}{2}, \quad v_x(1,s) = \frac{-2s}{2+s^2}, \quad v_y(1,s) = \frac{2\sqrt{2}}{2+s^2}, \tag{A7}$$

and that of $t(1,s)$ is the same as in the above.

All these expressions are at most cubic polynomials of s. Therefore they are numerically integrated with no truncation error if the order of the adopted integrator is greater than three such as the fourth order Runge-Kutta method. Again, the unregularized solution expressions are provided in terms of the above S-B solution expressions by solving the Kepler's equation, which reduces to a cubic equation named Barker's equation.

On the other hand, the B-F regularized solution is unchanged except for t, which is given as

$$t(1,f) = \sqrt{2}\tan\left(\frac{f}{2}\right) + \frac{\sqrt{2}}{3}\tan^3\left(\frac{f}{2}\right). \tag{A8}$$

A.3. Hyperbolic Orbit

The hyperbolic expressions are simply obtained from the elliptic ones by replacing the trigonometric functions with the corresponding hyperbolic functions for the arguments including s while taking care that $e > 1$. Thus the L-C and the S-B solutions become

$$u_1(e,s) = \cosh\left\{\frac{\left(\sqrt{e-1}\right)s}{2}\right\}, \quad u_2(e,s) = \sqrt{\frac{e+1}{e-1}}\sinh\left\{\frac{\left(\sqrt{e-1}\right)s}{2}\right\},$$

$$w_1(e,s) = \frac{\sqrt{e-1}}{2}\sinh\left\{\frac{\left(\sqrt{e-1}\right)s}{2}\right\}, \quad w_2(e,s) = \frac{\sqrt{e+1}}{2}\cosh\left\{\frac{\left(\sqrt{e-1}\right)s}{2}\right\},$$

$$t(e,s) = \frac{e\sinh\left\{\left(\sqrt{e-1}\right)s\right\} - \left(\sqrt{e-1}\right)s}{\left(\sqrt{e-1}\right)^3}, \quad r(e,s) = \frac{e\cosh\left\{\left(\sqrt{e-1}\right)s\right\} - 1}{e-1},$$

$$x(e,s) = \frac{e - \cosh\left\{\left(\sqrt{e-1}\right)s\right\}}{e-1}, \quad y(e,s) = \sqrt{\frac{e+1}{e-1}}\sinh\left\{\left(\sqrt{e-1}\right)s\right\},$$

$$v_x(e,s) = \frac{\sqrt{e-1}\sinh\left\{\left(\sqrt{e-1}\right)s\right\}}{e\cosh\left\{\left(\sqrt{e-1}\right)s\right\} - 1}, \quad v_y(e,s) = \frac{(e-1)\sqrt{e+1}\cosh\left\{\left(\sqrt{e-1}\right)s\right\}}{e\cosh\left\{\left(\sqrt{e-1}\right)s\right\} - 1}. \tag{A9}$$

Once again, the unregularized solution is given as $x(e,t) = x(e,s(e,t))$ and so on where $s(e,t)$ is obtained by solving the universal Kepler's equation.

Also, the B-F regularized solution is unchanged except for t, which is given as

$$t(e,f) = \frac{1}{\left(\sqrt{e-1}\right)^3}\left[\frac{e\sqrt{e^2-1}\sin f}{1+e\cos f} - 2\tanh^{-1}\left\{\sqrt{\frac{e-1}{e+1}}\tan\left(\frac{f}{2}\right)\right\}\right]. \tag{A10}$$

This time, the range of f is limited as $|f| < \pi - \tan^{-1}\sqrt{e^2-1}$, which assures that $\rho(e,f) > 0$ and the hyperbolic arctangent in the above is well-defined.

REFERENCES

Aarseth, S.J. 2003, Gravitational N-body simulations, (New York: Cambridge Univ. Press)

Arakida, H., & Fukushima, T. 2000, AJ, 120, 3333

Bond, V.R., & Allman, M.C. 1996, Modern Astrodynamics, (Princeton: Princeton Univ. Press)

Bürdet, C.A. 1967, Z. Angew. Math. Phys. 18, 434

Bürdet, C.A. 1968, Z. Angew. Math. Phys. 19, 345

Bürdet, C.A. 1969, J. Reine Angew. Math. 238, 71

Colwell, P., 1993, Solving Kepler's Equation Over Three Centuries, Willmann-Bell, Richmond, VA.

Ferrandiz, J.M. 1988, Celest. Mech. 41, 343

Fukushima, T. 1999, Celest. Mech. Dyn. Astron. 75, 201

Fukushima, T. 2003, AJ, 126, 1097

Fukushima, T. 2004, AJ, 128, 3114

Fukushima, T. 2005, AJ, 129, 2496

Fukushima, T. 2007, AJ, 133, 1

Heggie, D.C. 1973, in Recent Advances in Dynamical Astronomy, ed. B.D. Tapley & V. Szebehely (Dordrecht: Reidel), 34

Kustaanheimo, P., & Stiefel, E.L. 1965, J. Reine Angew. Math. 218, 204

Sperling, H. 1961, Am. Rocket Soc. Journal, 31, 1032

Stiefel, E.L., & Scheifele, G. 1971, Linear and Regular Celestial Mechanics, (New York: Springer)

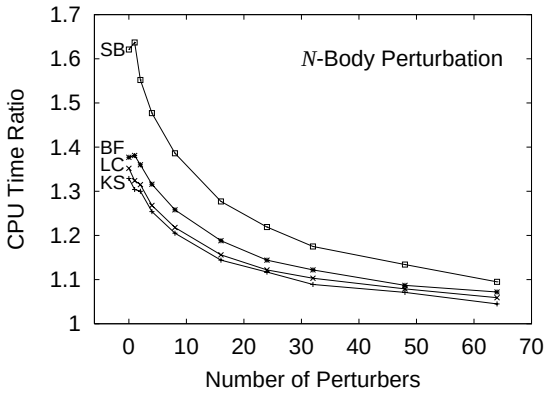

Fig. 1.— Computational time comparison of two-body regularizations. Shown are the ratios relative to that of the unregularized treatment. In the figure, 'SB' means the Sperling-Bürdet regularization, 'BF' does the Bürdet-Ferrandiz regularization, 'LC' does a three dimensional extension of Levi-Civita regularization, and 'KS' does the Kustaanheimo-Stiefel regularization. We omit the results of those with the Kepler enegy scaling since the differences due to the addition of the scaling are hardly visible.

This 2-column preprint was prepared with the AAS LaTeX macros v5.2.

TABLE 1

KEPLERIAN ELEMENTS ADOPTED FOR NUMERICAL EXPERIMENTS

Name	a (AU)	e	I (°)	Ω (°)	ω (°)	M_0 (°)	q (AU)	$\lambda \equiv (1-e)/(1+e)$
Icarus	1.078	0.827	22.9	88.1	31.3	323.8	0.1865	+0.0947
Jupiter	5.2026	0.0485	1.303	100.471	14.337	95.752	4.9503	+0.9075

TABLE 2

COMETS AND ASTEROIDS WITH LARGE ECCENTRICITIES

Object Type	ID (Name)	e	q (AU)	$\lambda \equiv (1-e)/(1+e)$
Hyperbolic Comets	C/1980 E1 (Bowell)	1.0558	3.377	−0.0271
	C/1997 P2 (Spacewatch)	1.0250	4.263	−0.0123
	C/1999 U2 (SOHO)	1.0243	0.049	−0.0120
	C/2002 Q3-A (LINEAR)	1.0228	1.309	−0.0113
Nearly Parabolic Comets	C/1973 E1 (Kohoutek)	1.000008	0.1424	-4.0×10^{-6}
	C/1962 C1 (Seki-Lines)	1.000003	0.0314	-1.5×10^{-6}
	C/2000 W1 (Utsunomiya-Jones)	0.9999997	0.3212	$+1.5 \times 10^{-7}$
	C/1910 A1 (Great January Comet)	0.999995	0.1290	$+2.5 \times 10^{-6}$
	C/1882 F1 (Wells)	0.999994	0.0608	$+3.0 \times 10^{-6}$
Unnumbered Asteroids	2005 VX3	0.99756	4.115	+0.00112
	2006 VZ13	0.99744	1.102	+0.00128
	2002 RN109	0.99566	2.691	+0.00217
	1996 PW	0.99003	2.518	+0.00501
Numbered Asteroids	87269 (2000 OO67)	0.96132	20.7661	+0.01972
	65407 (2002 RP120)	0.95503	2.4679	+0.02300
	20461 (Dioresta)	0.89972	2.3963	+0.05279
	3200 (Phaeton)	0.89005	0.1398	+0.05817

NOTE.—Selected are the top four or five objects in each category taken from the NASA/JPL Small-Body Database Search Engine. In choosing the nearly parabolic comets, we omit those assumed with pure parabolic orbits.

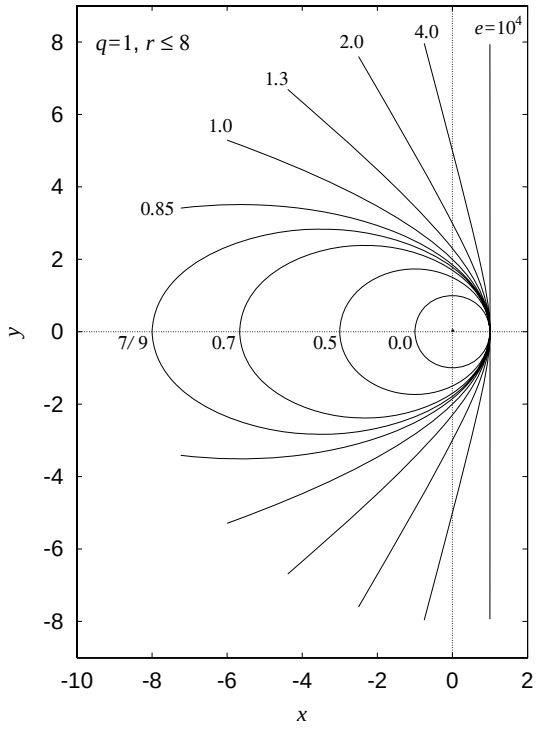

Fig. 2.— Sample orbits used for the close encounter experiment. Attached numbers are the orbital eccentricity, e. We use the arcs of orbits satisfying the condition $r \leq 8q$, where r and q are the radius vector and the pericenter distance, respectively. According to the value of eccentricity, the arcs are classified into two categories; open arcs and closed ellipses. The case of $e = 7/9$ is the critical case separating these two categories.

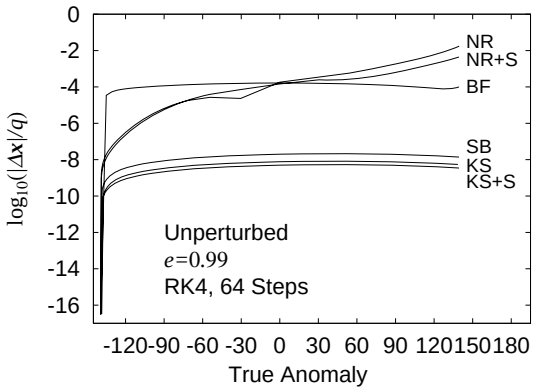

Fig. 3.— Integration error growth in one close encounter for an unperturbed nearly parabolic orbit with the eccentricity, $e = 0.99$. In the figure, 'NR' means the unregularized scheme and '+S' denotes the application of Kepler energy scaling. We omit the curve of a three-dimensional extension of the Levi-Civita regularization since it is practically the same as that of the Kustaanheimo-Stiefel regularization. This similarity is unchanged whether the Kepler energy scaling is applied or not. Note that the range of the true anomaly, f, is limited such that $r \leq 8q$; namely $|f| \leq \cos^{-1}[(e-7)/(8e)] \approx 139.362°$.

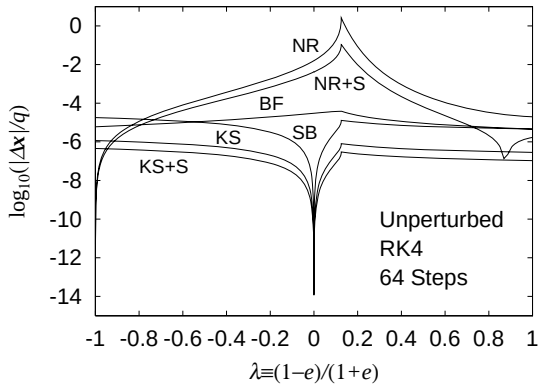

Fig. 4.— Eccentricity dependence of integration errors after one close encounter for unperturbed orbits. Again we omit the curves of a three-dimensional extension of the Levi-Civita regularization whether the Kepler energy application is applied or not since they are practically the same as those of the corresponding Kustaanheimo-Stiefel regularizations. The kinks of all the curves when $\lambda \equiv (1-e)/(1+e) = 0.125$ are due to the change of type of the tested orbit arc whether it is open (when $\lambda < 0.125$) or closed (when $\lambda \geq 0.125$). The reason of a kink of the curve 'NR+S' when $\lambda \sim 0.85$ is unclear to the author.

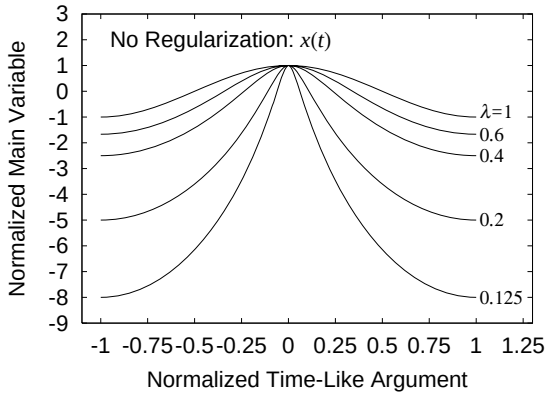

Fig. 5.— Variation of the pericenter-direction component of the position vector, x, in the unregularized treatment: closed arcs. Shown are the curves for closed arcs of orbits, namely in the case $0.125 \leq \lambda \leq 1$. The variable x is expressed in a unit system such that $\mu = q = 1$. The range of the physical time, t, is also normalized.

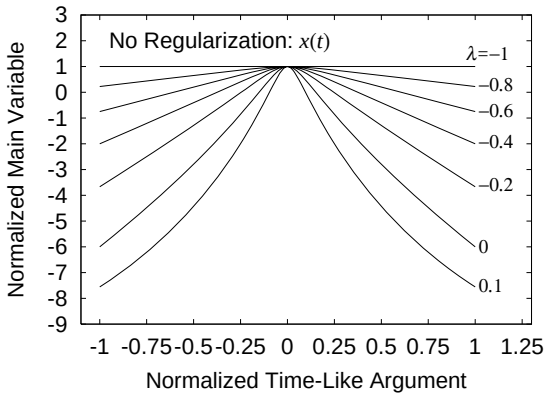

Fig. 6.— Variation of $x(t)$ in the unregularized treatment: open arcs. Same as Figure 5 but for open arcs of orbits, namely $-1 \leq \lambda < 0.125$. This time, the ranges of the physical time are limited such that $r \leq 8q$.

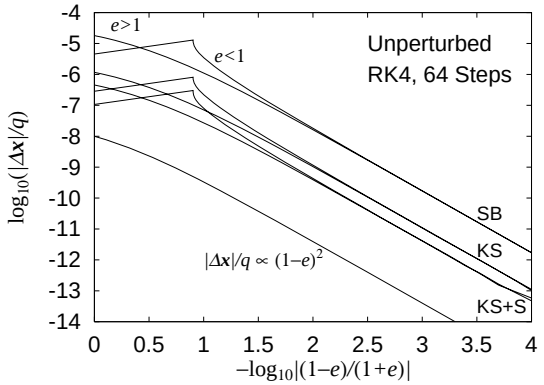

Fig. 7.— Closeup of some curves in Figure 4 expressed in a log-log scale with respect to $|(1-e)/(1+e)|$. Both the elliptic ($e < 1$) and the hyperbolic ($e > 1$) branches are shown together for the Sperling-Bürdet regularization and the Kustaanheimo-Stiefel regularization with and without the Kepler energy scaling. Once again we omit the curve of a three-dimensional extension of the Levi-Civita regularization whether the Kepler energy application is applied or not since they are practically the same as those of the corresponding Kustaanheimo-Stiefel regularizations. Also illustrated is a model curve of the eccentricity dependence of the global truncation errors of the associated harmonic oscillation by a fourth order integrator.

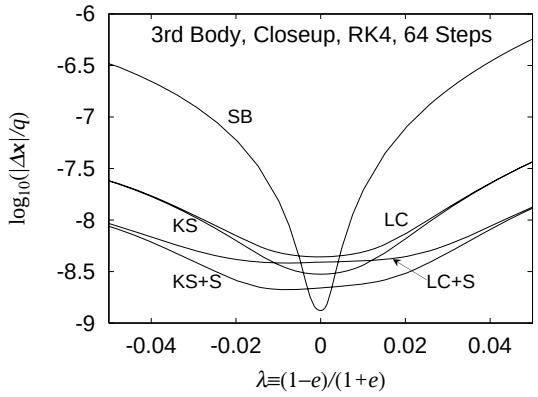

Fig. 8.— Same as Figure 4 but under the third body perturbation. We omit the results of the Bürdet-Ferrandiz regularization and of the unregularized treatments with and without the Kepler energy scaling since they are of less performance. Only the region near $\lambda \sim 0$ is magnified.

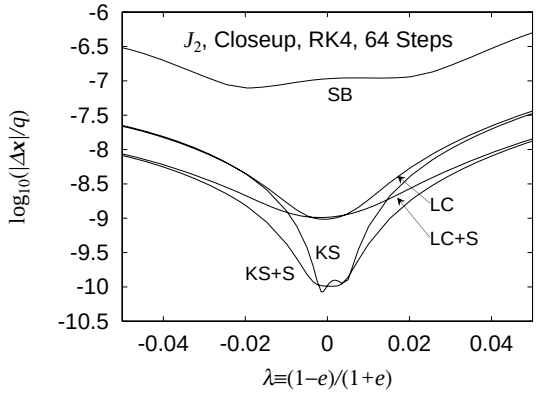

Fig. 9.— Same as Figure 8 but under the J_2 perturbation.

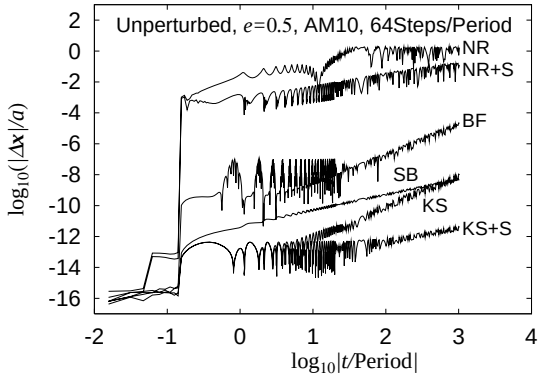

Fig. 10.— Growth of integration errors for an unperturbed elliptic orbit. We omit the curves of the extended Levi-Civita regularization with and without the Kepler energy scaling since they are practically the same as those of the corresponding Kustaanheimo-Stiefel regularizations.

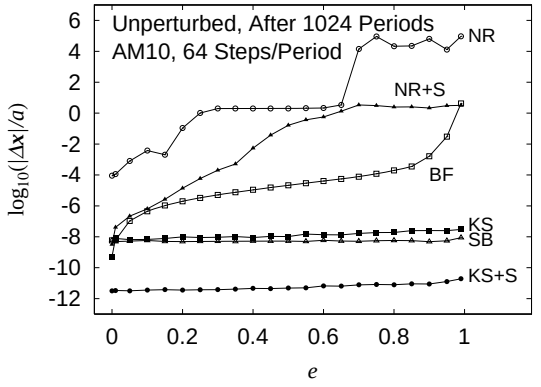

Fig. 11.— Eccentricity dependence of integration errors for unperturbed elliptic orbits after 1024 orbital periods. This time, the errors are normalized by not q but a. The tested eccentricities are 0.0, 0.01, 0.05, 0.10, 0.15, ..., 0.95, and 0.99. Again we omit the curves of the extended Levi-Civita regularizations with and without the Kepler energy scaling.

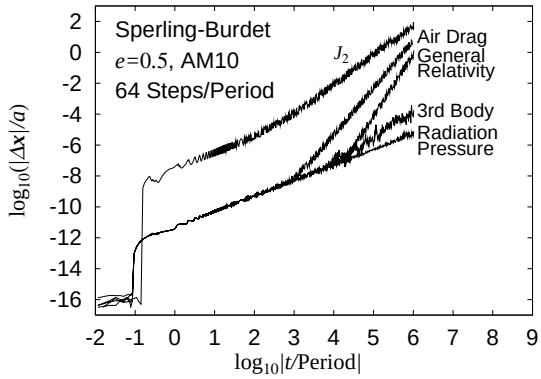

Fig. 12.— Perturbation type dependence of the integration error growth of the Sperling-Bürdet regularization. The perturbations tested are the third body perturbation, the air drag perturbation, the general relativity perturbation, the radiation pressure perturbation, and the J_2 perturbation.

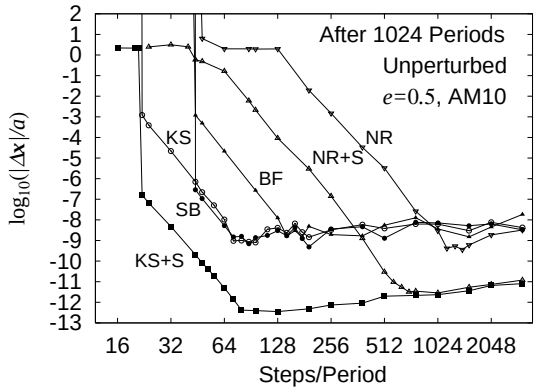

Fig. 13.— Cost performance diagram for an unperturbed elliptic orbit; $e = 0.5$. Once again we omit the curves of the extended Levi-Civita regularization with and without the Kepler energy scaling since they are practically the same as those of the corresponding Kustaanheimo-Stiefel regularizations.